PHOTONICS Research

Enhancing THz fingerprint detection on the planar surface of an inverted dielectric metagrating

Xueying Liu,[1,2] Wei Chen,[1] Yongjie Ma,[1] Yinong Xie,[1] Jun Zhou,[3] Liguo Zhu,[4] Yadong Xu,[5] AND Jinfeng Zhu[1,2,*]

[1]*Institute of Electromagnetics and Acoustics and Key Laboratory of Electromagnetic Wave Science and Detection Technology, Xiamen University, Xiamen 361005, China*
[2]*State Key Laboratory of Applied Optics, Changchun Institute of Optics, Fine Mechanics and Physics, Chinese Academy of Sciences, Changchun 130033, China*
[3]*Terahertz Research Center, University of Electronic Science and Technology of China, Chengdu 610054, China*
[4]*Microsystem and Terahertz Research Center, China Academy of Engineering Physics, Mianyang 621900, China*
[5]*School of Physical Science and Technology and Institute of Theoretical and Applied Physics, Soochow University, Suzhou 215006, China*
*Corresponding author: nanoantenna@hotmail.com

Terahertz (THz) molecular fingerprint sensing provides a powerful label-free tool for the detection of trace-amount samples. Due to the weak light–matter interaction, various metallic or dielectric metasurfaces have been adopted to enhance fingerprint absorbance signals. However, they suffer from strong background damping or complicated sample coating on patterned surfaces. Here, we propose an inverted dielectric metagrating and enhance the broadband THz fingerprint detection of trace analytes on a planar sensing surface. Enhancement of the broadband signal originates from the effects of evanescent waves at the planar interface, which are excited by multiplexed quasi-bound states in the continuum (quasi-BICs). One can evenly boost the near-field intensities within the analytes by tuning the asymmetry parameter of quasi-BIC modes. The multiplexing mechanism of broadband detection is demonstrated by manipulating the incident angle of excitation waves and thickness of the waveguide layer. Compared to the conventional approach, the THz fingerprint peak value is dramatically elevated, and the largest peak enhancement time is 330. Our work gives a promising way to facilitate the meta-sensing of the THz fingerprint on a planar surface and will inspire universal THz spectral analysis for trace analytes with different physical states or morphologies.   © 2022 Chinese Laser Press

https://doi.org/10.1364/PRJ.472114

1. INTRODUCTION

Terahertz (THz) spectroscopy provides a non-invasive and label-free sensing tool for many kinds of chemical and biological materials, because their molecular fingerprint spectra reflect specific intra- and intermolecular vibrations for sample identification [1–3]. In trace-amount detection, conventional THz sensing faces the challenge of weak light–matter interactions due to the dimension mismatch between the wavelength and sample scale [4–6]. The use of metasurfaces in THz sensing can effectively overcome this problem by powerful light confinement. In the past few years, sensing based on metallic metasurfaces has been intensively investigated to enhance THz wave interaction and trace detection sensitivity by using their near-field effects [7–10]. In fact, these metasurfaces not only bring about serious background signal interference originating from high ohmic dissipation of metal, but also enhance the detection signal in a narrow band. They cannot well meet a comprehensive analysis of multiple frequency features in a wide fingerprint

spectrum. On this occasion, a low-loss broadband metasurface sensor is quite in demand.

Recently, the use of all-dielectric metasurfaces has demonstrated great potential in enhancing molecular fingerprint detection, since dielectric materials typically have much lower optical losses versus metals [11–14]. Tittl *et al.* have reported broadband mid-infrared fingerprint sensors based on all-dielectric metasurfaces by using quasi-bound states in the continuum (quasi-BICs) [15,16], which has provided significant research guidance for all-dielectric metasurface sensing in a wide THz band. BICs in all-dielectric metasurfaces represent perfect bound states embedded in a radiative continuum without radiation leakage, and they enable infinite quality (Q) factors [17–19]. Ideal BICs are typically not observable. Notably, by breaking the structure symmetry in all-dielectric metasurfaces, ideal BICs can be transformed into quasi-BICs, which support a series of ultra-high Q resonances. They can be utilized in broadband fingerprint sensing for trace samples coated on the

metastructure by a multiplexing mechanism [20]. Despite the pioneering work of all-dielectric metasurfaces in mid-infrared quasi-BIC fingerprint metasensing, the THz metastructure (typically 5–50 μm in height) has a much larger surface undulation than the mid-infrared counterpart (typically <1 μm in height). It requires complicated and dedicated interface engineering for conformal coating of ultra-thin trace-amount analytes (1 nm–1 μm) on the metastructure. Actually, such a sample coating on top of the THz metastructure limits its universality of quasi-BIC metasensing for various trace analytes, because the samples usually have many kinds of physical states or morphologies, such as powder, viscous liquid, randomly distributed biomolecules, and 2D materials. Additionally, even though one can accomplish a perfect conformal sample coating, the enhanced fingerprint absorption on the entire sample surface should not be uniform as a result of inhomogeneous electric field intensity distributions, which might seriously lower the efficiency of light–matter interaction for sensing. Therefore, it is of great importance to design a universal quasi-BIC metasensor with high sensing efficiency for elevating the broadband THz molecular fingerprint detection of trace analytes.

In this paper, we propose a high-performance universal metasensor based on broadband reconfigurable quasi-BICs, which facilitates THz molecular fingerprint detection of various trace-amount analytes coated on a planar sensing surface. In our design, the multiplexed THz-wave excitations are applied on an all-dielectric metastructure, and the ultra-thin trace analytes can be coated on the planar surface opposite to the metastructure and detected by a series of reflective spectra. We illuminate the metasensing mechanism by a set of systematic theoretical analysis and optical simulations. Specifically, we find that each quasi-BIC mode induces an evanescent field at the interface between air and the planar surface, where the THz absorption of trace samples is enhanced significantly. By using the signals of multiplexed incident angles or dielectric waveguide (WG) thicknesses, we dramatically boost the THz molecular fingerprint of trace analytes. The planar sensing surface is more flexible than the patterned surface for detecting ultra-thin trace samples of various physical states or morphologies. By tuning the asymmetry parameters of quasi-BICs, the detection performance is improved considerably. Our study denotes a convenient and universal platform for high-sensitivity detection of trace THz molecular fingerprints, and will also inspire more THz sensing applications of nanoscale analytes.

2. DESIGN AND METHODS

According to the breaking principle of symmetry-protected BICs [21–23], the design of the quasi-BIC metasensor based on a homogeneous SiO$_2$ dielectric metastructure is illustrated in Fig. 1. A unit cell of the metastructure has period p and consists of a four-element asymmetric subwavelength grating layer located below a WG layer. In the grating layer, the first and third elements are the material of SiO$_2$ with the same width $w_1 = w_3 = w_0 = p/4$. The second and fourth elements are air with widths of $w_2 = w_0 + \Delta w$ and $w_4 = w_0 - \Delta w$, where the size tuning factor Δw can take values from 0 μm to w_0. Thus, we can define a structure asymmetry parameter $\eta = \Delta w / w_0 \in [0, 1]$ to reflect the size difference between
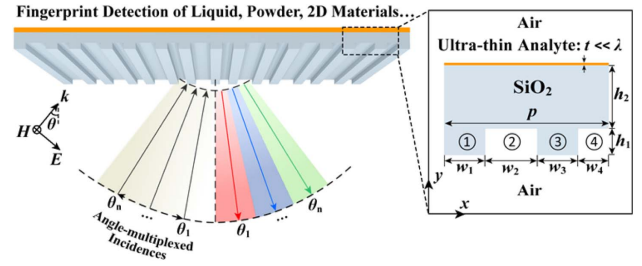
Fig. 1. Schematic drawing of THz molecular fingerprint sensing on a planar surface, where the all-dielectric metastructure supports a series of quasi-BICs by using angle-multiplexed signals. The symbols w_1, w_2, w_3, and w_4 denote the widths of four grating elements, while p, h_1, and h_2 represent the unit cell period, grating layer height, and WG layer height, respectively.

the second and fourth elements of air. The heights of the grating layer and WG layer are h_1 and h_2, respectively. The dielectric material of SiO$_2$ is assumed to be nonmagnetic ($\mu = \mu_0$), and its THz optical parameters are obtained from the literature [24]. The angle-multiplexed incidences of transverse magnetic (TM) THz waves are adopted on the metastructure, and the ultra-thin trace samples with thickness t can be coated on the inverse planar side of the metastructure. To reveal the sensing physics comprehensively, numerical simulations of optical models are carried out based on the rigorous coupled-wave analysis and finite element method based on COMSOL Multiphysics [25]. In the simulations, Floquet boundary conditions are used for the periodic unit cells. Since the thickness of the trace analyte layer is much smaller than the THz wavelength, the equivalent transition boundary condition can be applied to the analyte layer to reduce the meshing number and simulation time.

3. RESULTS AND DISCUSSION

A. Generation of Evanescent Waves on a Planar Surface by Quasi-BICs

To interpret the formation mechanism of quasi-BICs, we preliminarily study the dispersion relation for the all-dielectric metasensor with $\eta \neq 0$ and plot it in Fig. 2(a). For the incident medium of air, it is defined by the in-plane wave vector component $k_x = k_0 \cdot \sin \theta$, where θ is the angle of incidence, and $k_0 = \omega/c$ is the free-space wavenumber. For the metastructure, k_x inside the WG layer for the mth diffraction order can be determined by $k_x = k_0 \cdot \sin \theta - m \cdot 2\pi/p$ ($m = \pm 1, \pm 2, \ldots$), where $G_x = m \cdot 2\pi/p$ denotes the reciprocal lattice vector induced by the grating. Since the metastructure is a periodic grating, it leads to the translation symmetry of the band structure in reciprocal space. Due to the band folding, the WG light line can fall above the air light line at some specific frequencies, which leads to coupling from the incoming light to the guided modes of the WG layer. Such guided-mode resonances (GMRs) can be excited when the propagation constant β satisfies the following phase matching conditions [26,27]:

$$k_x = k_0 \sin \theta - m \frac{2\pi}{p} = \beta \quad (m = \pm 1, \pm 2, \ldots). \quad (1)$$
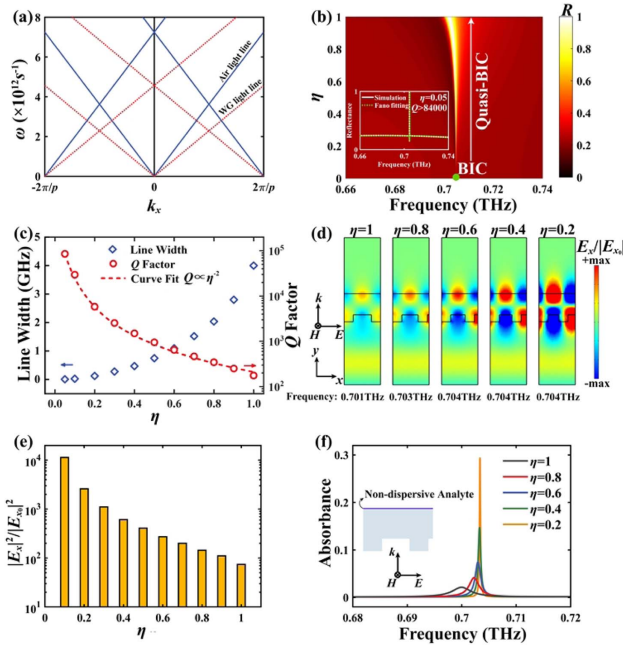
Fig. 2. (a) Dispersion relations in the WG layer for the fundamental mode of TM wave and in the air. (b) Reflectance (R) of a bare metastructure as a function of frequency and asymmetry parameter. The inset is the reflectance spectrum of $\eta = 0.05$ fitted by the Fano equation. (c) Linewidth and Q factor as functions of η. (d) Normalized electric field E_x distributions at corresponding resonance frequencies. (e) Maximum local electric field enhancement at the planar interface. (f) Absorbance of the metastructure with a perturbation analyte layer 1 μm thick, whose refractive index is $\tilde{n} = 1.5 + 0.05i$. All metastructures are under normal incidence with $p = 260$ μm, $w_1 = w_3 = 65$ μm, $w_0 = 65$ μm, $h_1 = 50$ μm, and $h_2 = 150$ μm.

The dispersion relation in the WG layer for the GMR mode of TM wave excitation can be solved by rigorous calculation as [26,27]

$$d\sqrt{k_0^2 n^2 - \beta^2} = 2 \arctan\left(\frac{n^2}{n_{air}^2}\sqrt{\frac{\beta^2 - k_0^2 n_{air}^2}{k_0^2 n^2 - \beta^2}}\right), \quad (2)$$

where d is the thickness of the WG layer, and n and n_{air} are the refractive indices of the WG layer and air, respectively. In the situation of $\eta = 0$, the metasensor with period p degenerates to a metastructure with half-period $p/2$, the grating-induced reciprocal lattice vector G'_x changes to $m \cdot 4\pi/p$, and the phase matching condition of GMR is destroyed. When $\eta \neq 0$, the odd-order GMR is excitable in the metastructure, but it cannot be excited in the metastructure of $\eta = 0$ and transforms into a discrete dark mode with zero-resonance width and infinite Q factor, which is called BIC [23]. To reveal the resonance mode transformation from $\eta = 0$ to $\eta \neq 0$, we plot the reflectance (R) of a bare metastructure as a function of frequency and an asymmetry parameter in Fig. 2(b). The green dot in this figure denotes the critical frequency location (∼0.704 THz) of the BIC for $\eta = 0$, where the dark-mode resonance is not observable. When the value of η becomes a positive perturbation of 0.05, we can observe a remarkable resonance peak

around the frequency of ∼0.704 THz in the inset of Fig. 2(b). This kind of resonance for $\eta \neq 0$ belongs to a leaky guided mode that is strongly confined and localized, and it is usually called quasi-BIC. The corresponding spectral profile shows an asymmetric feature, which can be fitted by Fano resonance theory as [28–30]

$$R(\omega) = R_0 + C_0 \frac{[q + 2(\omega - \omega_0)/\tau]^2}{1 + [2(\omega - \omega_0)/\tau]^2}, \quad (3)$$

where R_0, C_0, and q are the reflectance offset, continuum discrete coupling constant, and Breit–Wigner–Fano parameter, respectively. ω_0 is the resonance frequency, τ characterizes the linewidth of the resonance, and ω represents the frequency in the THz region. The Q factor of the resonance is calculated by $Q = \omega_0/\tau$. To obtain it, we fit the reflectance spectra to Eq. (3) for different η values (see details in Appendix A). As observed in Fig. 2(b), quasi-BICs have almost the same central frequency of resonance. Their resonance linewidths rise from 0.008 to 4 GHz as the value of η increases from 0.05 to 1 in Fig. 2(c). The Q factor reduces dramatically from 84,908 to 175 as η changes from 0.05 to 1. In fact, the series of quasi-BIC Q factors implies the inverse square dependence on η and can be well fitted by the equation $Q = Q_0 \cdot \eta^{-2}$, where Q_0 is 210 [21].

Furthermore, we investigate the electric field distributions of quasi-BICs and plot them in Fig. 2(d). It shows that the electric field is induced by the leaky guided mode and confined along the upper and lower surfaces of the entire metastructure. Particularly, the field distributions indicate that there are evanescent waves at the planar interface between the WG layer and air for resonance frequencies (e.g., the field decay length for $\eta = 0.8$ is about 51 μm). The electric fields are enhanced along with the planar interface, and their intensities gradually increase as η changes from 1 to 0.2, as shown in Fig. 2(d). We calculate the enhancement for the maximum localized electric field at the planar interface in Fig. 2(e), which shows that the field enhancement factor increases from 74 to 11,364 with η changing from 1 to 0.1. The high enhancing efficiencies of the evanescent field suggest a strong sensing potential for the detection of trace-amount analytes coated on the interface. In the next simulation, we coat an analyte layer 1 μm thick as a perturbation on the planar interface and obtain the absorbance spectra for different values of η in Fig. 2(f). The analyte is non-dispersive with a complex refractive index of $\tilde{n} = 1.5 + 0.05i$. The THz absorbance of the analyte can be determined by the following equation [31]:
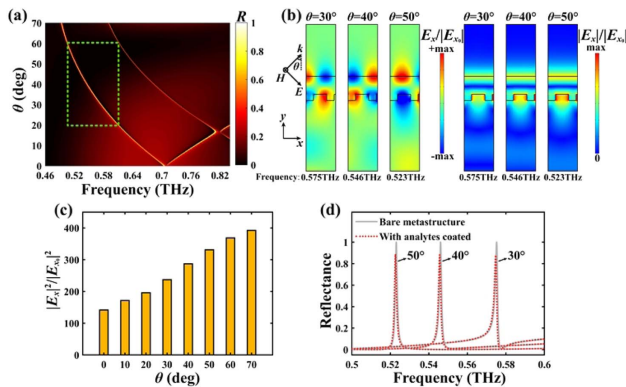
$$A = 4\pi f n k \int_V |E_l|^2 \, dV, \quad (4)$$

where n and k represent the refractive index and extinction coefficient of the analyte, respectively, V is the volume of the analyte, and E_l denotes the local electric field component in the analyte. Due to the interface electric field increasing significantly along with the decrease of η, we can observe that the absorbance peak value of the analyte elevates prominently in Fig. 2(f), which is consistent with Eq. (4). The Q factor of the absorbance peak becomes larger with the reduction of η, which is consistent with the result in Fig. 2(c). Figure 2(f) also elucidates that the absorbance of the non-dispersive analyte is

almost zero when the frequency stays far from the resonance point, which is attributed to the disappearance of evanescent waves and near-field enhancement.

B. Angle-Multiplexed Quasi-BIC Sensing Mechanism and Fingerprint Detection

Based on the above quasi-BIC studies under normal incidence, we next investigate the THz responses of different incident angles. The reflectance of quasi-BIC as a function of incident angle θ and frequency for $\eta = 0.8$ is plotted in Fig. 3(a). It indicates multiple narrow reflectance bands, which correspond to a series of quasi-BICs implied in the phase matching condition of Eq. (1). Particularly, as observed in the frame of the green dashed line for the fundamental mode of $m = +1$, the frequency of maximum reflectance (from 0.505 to 0.611 THz) increases monotonically as θ reduces from 60° to 20°. This result demonstrates that one could simply tune the THz quasi-BICs by a one-to-one mapping of incident angles and frequencies. We continue to plot the field distributions of quasi-BICs under different incident angles in Fig. 3(b). The normalized electric field distributions under oblique incidence ($\theta = 30°$, 40°, or 50°) exhibit the very similar features of evanescent waves to those under normal incidence. In fact, the electric field is also enhanced considerably, and the intensity enhancement is homogeneous along with the planar interface. The electric field enhancement factors at the interface under a series of incident angles are calculated in Fig. 3(c). It exhibits a gradual rise from 144 to 392 as θ increases from 0° to 70°. If we coat a trace-amount analyte layer on the planar interface, such electric field distributions for various values of θ would inherit the great THz absorption capability. To evaluate the absorption enhancement levels for different values of θ, we introduce a non-dispersive analyte layer 1 μm thick as a perturbation on the interface and compare the reflectance spectra in Fig. 3(d). It indicates almost the same peak reduction for the angle-dependent reflectances, which can be explained by using

the absorbance calculation of Eq. (4). Although the electric field intensity becomes larger with the increase of θ [see Fig. 3(c)], the resonance frequency becomes smaller with θ increasing [see Fig. 3(a)]. This leads to almost the same decline of reflectance peaks at different angle-dependent resonance frequencies. The property implies that the use of angle-multiplexed reflectance spectra can effectively achieve consistent peak absorbance enhancement levels for each frequency sampling point. It is very promising for the metasensing of the broadband molecular fingerprint with multiple frequency features.

After discussing the sensing enhancement around resonance frequency points, we continue to evaluate the metasensing performance for ultra-thin dispersive analytes. Here, α-lactose is adopted as the analyte to be detected, and its dispersive THz parameters are provided in Fig. 4(a) [32]. To reveal the potential of our metasensing, we systematically compare the effects of three sample coating cases on fingerprint detection performance, as illustrated in Fig. 4(a). In the simulation, the sample volumes for different coatings are the same with thicknesses of 0.56 μm (case I), 1 μm (case II), and 1 μm (case III). Before the sample loading, there is a series of single sharp reflectance spectra by using multiplexed incident angles from 28° to 71°, as shown in Fig. 4(b). All peak values of these reflectance spectra are near unity, and we can draw the envelope
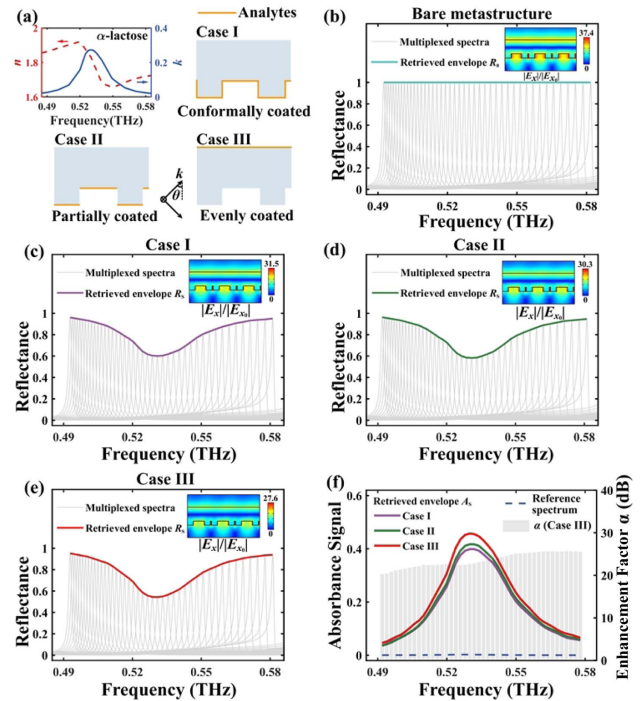
Fig. 4. (a) Complex refractive index of α-lactose and its three surface coating cases for equal volumes of trace samples. The angle-multiplexed reflectance spectra and their envelopes are provided for (b) a bare metastructure, (c) case I, (d) case II, and (e) case III, where each inset denotes the normalized electric field distribution for the minimum reflectance peak at $\theta = 46°$. (f) Absorbance envelopes of three cases and the sensing enhancement factors versus a reference spectrum for case III. For all simulations, the metastructure parameters are $p = 260$ μm, $\eta = 0.8$, $w_1 = w_3 = 65$ μm, $w_2 = 117$ μm, $w_4 = 13$ μm, $h_1 = 50$ μm, $h_2 = 150$ μm, and θ changes from 28° to 71°.

Fig. 3. (a) Reflectance of a bare metastructure as a function of frequency and θ. (b) Normalized electric field distributions at resonance frequencies under different θ values. (c) Maximum local electric field enhancement at the planar interface for different θ values. (d) Reflectance before and after introduction of a perturbation analyte layer ($\tilde{n} = 1.5 + 0.05i$) 1 μm thick at the planar interface for different θ values. For all simulations, the metastructure parameters are $p = 260$ μm, $\eta = 0.8$, $w_1 = w_3 = 65$ μm, $w_2 = 117$ μm, $w_4 = 13$ μm, $h_1 = 50$ μm, and $h_2 = 150$ μm.

of peaks as R_0 and assume it as a blank reference for fingerprint sensing. The reflectance spectra and peak envelopes (R_s) for the three sample coating cases are plotted in Figs. 4(c), 4(d), and 4(e), respectively. All sample-induced peak envelopes for the three cases have a dip at around 0.53 THz, which corresponds to the frequency of the maximum THz extinction coefficient for α-lactose. These results indicate that the three types of envelopes by multiplexed-angle signals can well reflect the α-lactose molecular fingerprint feature. To quantify the retrieved absorbance features of trace samples, we calculate their absorbance envelopes (A_s) according to the following equation:

$$A_s(f) = 1 - R_s(f)/R_0(f). \qquad (5)$$

Their retrieved envelopes are plotted in Fig. 4(f), and we can observe that the peaks of absorbance envelopes for all three cases are the same at 0.53 THz. These envelope signals are enhanced significantly compared to that of conventional sensing, in which the analyte is coated on an unpatterned SiO$_2$ substrate 200 μm thick. The absorbance obtained by conventional sensing is the reference absorbance spectrum, as the blue dashed line shows in Fig. 4(f). For instance, the envelope signal intensities at around 0.53 THz are elevated from 0.25% (reference spectrum) to 39.8% (case I), 41.7% (case II), and 45.7% (case III). Although the fingerprint information of α-lactose can be retrieved for the three cases, case III has the best fingerprint signal enhancement. This can be explained by the electric field distributions for $\theta = 46°$ and $f = 0.53$ THz in the insets of Figs. 4(b)–4(e). The corresponding enhanced field is concentrated not only inside the grooves of the bottom metasurfaces, but also on the top planar interface. The introduction of the analyte leads to the absorption of THz waves and reduces the surrounding electric field intensity at the resonance frequency. By taking the inset in Fig. 4(b) as a reference, the reduction of electric field intensity in Fig. 4(e) is larger than those in Figs. 4(c) and 4(d). According to Eq. (4), the spatial volume infinitesimal distributions of samples in cases I and II lead to lower intensities of effectively utilized field and smaller field volume integral values. The higher absorption efficiency of case III is attributed to the more uniform field applied on the analyte and the larger effective field volume integral. To quantify the broadband detection enhancement, we define the frequency-dependent absorption enhancement factor as

$$\alpha = 10 \lg \left[\frac{\int_{f_1}^{f_2} A(f)\mathrm{d}f}{\int_{f_1}^{f_2} A_{\mathrm{ref}}(f)\mathrm{d}f} \right], \qquad (6)$$

where $A(f)$ and $A_{\mathrm{ref}}(f)$ are the frequency-dependent absorbance of the analyte on the metasensor and the unpatterned SiO$_2$ substrate with the same thickness, respectively. f_1 and f_2 represent the starting and ending points of a frequency interval, respectively. We calculate the enhancement factors of case III as the gray histogram in Fig. 4(f), which are all above 20.3 dB. In practical detection, it is much more convenient for case III with a planar sensing surface to implement interface engineering for THz trace sensing. This makes our design very attractive and universal for sensing applications of various physical states or morphologies for trace samples.

To emphasize the advantages of quasi-BIC tuning, we compare the detection performance with the traditional GMR

metastructure (namely, $\eta = 1$). Figure 5(a) shows the fingerprint absorbance spectrum of α-lactose measured by the conventional sensing method. The spectral absorbance of 1 μm thick α-lactose by conventional sensing is less than 0.25%, and its molecular fingerprint cannot be identified. On the contrary, the retrieved fingerprint signals by the angle-multiplexed metasensing on a planar surface are much more remarkable for 1 μm thick α-lactose, as shown in Fig. 5(b). When η equals one (traditional GMR), the absorbance at the fingerprint feature of 0.53 THz is 31.4%, which is comparable to the intensity of a 76 μm thick sample layer by conventional sensing. As η decreases from 1 to 0.4, the fingerprint peak value at 0.53 THz is elevated to 84.4%, which is comparable to that of a 395 μm thick sample layer by conventional sensing. The absorbance intensity demonstrates 330 times enhancement versus the conventional sensing spectrum of 1 μm thick α-lactose. These results imply that one can tune quasi-BIC modes to enhance the detection of a trace-amount analyte with a low THz extinction coefficient. To elucidate the universality of this metasensing approach, we explore the detection of a representative 2D material, namely, reduced graphene oxide (rGO), with an extremely small thickness of 20 nm. The real part of dispersive conductivity in Fig. 5(c) exhibits two obvious peak features at frequencies of about 0.94 and 1.02 THz [33]. By engineering the incident angles from 22° to 59°, we obtain remarkable fingerprint absorption envelope signals by using an optimized asymmetry parameter of 0.6 in Fig. 5(d). The reference absorbance for the conventional sensing is very low with a fingerprint peak value less than 0.48%. The absorbances at the two feature points increase extraordinarily from 0.48% and 0.21% (reference spectrum) to 62.5% and 51.4% (retrieved
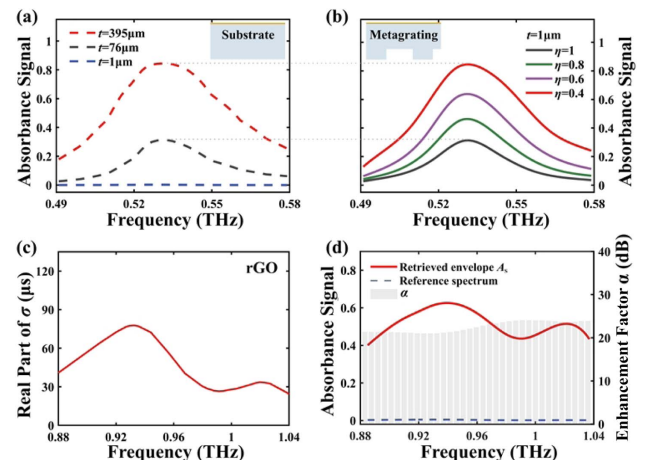
Fig. 5. (a) Absorbance spectra of α-lactose with different thicknesses by conventional sensing. (b) Retrieved absorbance signals of 1 μm α-lactose by the angle-multiplexed metasensing method. For the simulation of α-lactose, the metastructure parameters are $p = 260$ μm, $w_1 = w_3 = 65$ μm, $h_1 = 50$ μm, $h_2 = 150$ μm, and θ changes from 28° to 71°. (c) Real part conductivity of 20 nm thick rGO. (d) Absorbance envelope of 20 nm thick rGO and the broadband enhancement factors versus a reference absorbance spectrum. For the simulation of rGO, the metastructure parameters are $p = 130$ μm, $\eta = 0.6$, $w_1 = w_3 = 32.5$ μm, $w_2 = 58.5$ μm, $w_4 = 6.5$ μm, $h_1 = 50$ μm, $h_2 = 150$ μm, and θ changes from 22° to 59°.

envelop A_s), respectively. In this frequency range, the absorption enhancement factors are all larger than 21 dB. In addition, the thickness h_2 of the WG layer is also important for sensing performance. We investigate its effects on THz fingerprint angle-multiplexed metasensing (see details in Appendix B). Therefore, the proposed metasensing method would enable many applications for the THz fingerprint detection of ultra-thin analytes and 2D materials.

C. Thickness-Multiplexed Quasi-BIC Sensing of Trace-Amount THz Fingerprint

In addition to the angle-multiplexed sensing scheme, we can also tune quasi-BIC modes by manipulating the WG layer thickness, which can provide an alternative degree of freedom by microfluidic control for broadband THz fingerprint detection. Notably, this method supports the fixed normal incidence, which could facilitate the operation of optical measurement. A schematic drawing of the proposed device is shown in Fig. 6(a). The metasensor with unit cell period p consists mainly of SiO_2, Topas, and trans-decalin, whose THz optical parameters are obtained from the literature [24,34,35]. The thickness of the grating layer is h_1. SiO_2 is adopted as the first and third material elements for the grating layer with the same width $w_1 = w_3 = w_0 = p/4$. Topas is used as the second and fourth material elements with widths of $w_2 = w_0 + \Delta w$ and $w_4 = w_0 - \Delta w$. Thus, the asymmetric geometric parameter is also $\eta = \Delta w/w_0 \in [0, 1]$. The microfluidic channel with a tunable thickness of h_2 is filled with the trans-decalin. Additionally, two SiO_2 layers with a fixed thickness d of 10 μm are configured to sandwich the microfluidic channel layer, which can prevent direct contact between the analyte and trans-decalin. The metasensor can be fabricated based on the microelectromechanical systems technique [36,37]. The normal incidence of TM waves from the bottom is adopted.

To demonstrate the function of the microfluidic channel, we investigate the influence of channel thickness h_2 on THz quasi-BIC modes. Here, we take $\eta = 0.8$ as a paradigm and simulate the reflectance of THz waves in the frequency range of 2–2.8 THz. In Fig. 6(b), there are more and more reflectance bands of quasi-BIC modes as h_2 increases from 0 to 200 μm. According to Eq. (2), the resonance frequency shifts with the change of h_2. By simply changing the channel thickness h_2, one can flexibly tune the peak position of reflectance in a wide THz band, which would facilitate broadband fingerprint detection. At the frequency of 2.7 THz, there are four reflectance peaks for channel thicknesses of 9, 64, 119, and 174.4 μm. Their normalized electric field distributions are plotted in Fig. 6(c), all of which exhibit almost the same evanescent field feature at the top metastructure–air interface. Such interface field distributions are much like that in the angle-multiplexed metasensor in Fig. 3(b). The enhanced electric field along the planar surface is beneficial for the fingerprint signal enhancement of ultra-thin materials or 2D materials. The field decay length away from the top layer is long enough (42 μm), which could ensure a strong light–matter interaction for the coated trace-analyte layer. By changing h_2 from 0 to 200 μm at intervals of 5 μm, a series of sharp reflectance spectra for the bare metastructure is illustrated in Fig. 6(d). The values of these peaks are almost unity for the R_0 envelope, which could be used as the
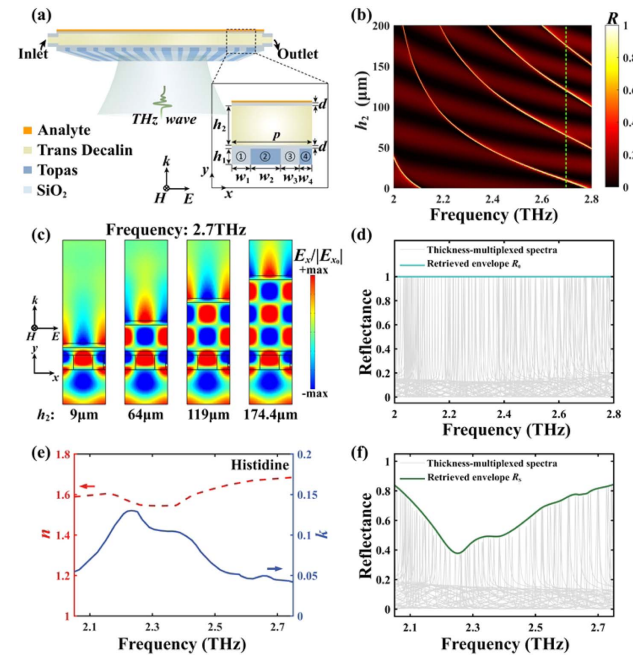
Fig. 6. (a) Schematic drawing of the THz quasi-BIC all-dielectric metasensor using a thickness-multiplexed sensing scheme. (b) Reflectance as a function of frequency and thickness h_2. (c) Field distributions for resonance peaks at a frequency of 2.7 THz. (d) Thickness-multiplexed (tunable h_2) reflectance spectra and envelope for an unloaded metasensor. (e) Complex refractive index of histidine. (f) Reflectance spectra and envelope of coating 1 μm thick histidine on the metasensor. The normal incidence of THz waves is applied on the metastructure, whose parameters are $p = 105$ μm, $\eta = 0.8$, $w_1 = w_3 = 26.25$ μm, $w_2 = 47.25$ μm, $w_4 = 5.25$ μm, and $h_1 = 35$ μm.

original reference signal before fingerprint detection. To assess the trace detection performance of this metasensor, we coat 1 μm thick histidine, whose THz optical parameters are shown in Fig. 6(e) [38]. The thickness-multiplexed reflectance spectra and their peak envelope R_s of coating the trace histidine on the planar surface are plotted in Fig. 6(f). Referring to Fig. 6(e), such an envelope clearly reflects the fingerprint features of histidine. This indicates that the thickness-multiplexed metasensing scheme can also effectively retrieve the THz molecular fingerprint of trace analytes.

We next study the trace sensing performance of thickness-multiplexed metasensors. With the demonstration in Figs. 2(d)–2(f), the asymmetric parameter η can bring about a critical impact on the field intensity at the top metastructure–air interface. In Fig. 7(a), we plot the electric field distributions at $f = 2.7$ THz for four bare metastructures with various η values of 1, 0.8, 0.6, and 0.4. The surface near-field intensity increases as η reduces. We compare the detection signals of 1 μm thick histidine for different η of 1, 0.8, 0.6, and 0.4. The absorbance envelopes from the reflectance spectra are shown in Fig. 7(b). Compared with the reference spectrum obtained by conventional detection, the sensing envelope signals by the thickness-multiplexed method are significantly enhanced for different η, and the absorption intensities increase gradually with
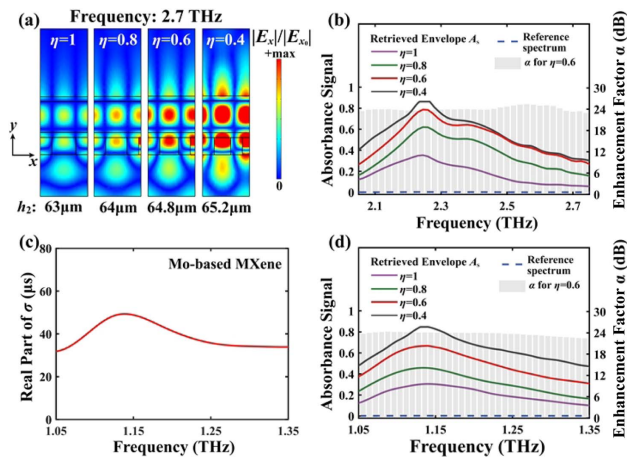
Fig. 7. (a) Normalized electric field distributions of unloaded metastructures at $f = 2.7$ THz for different values of η. (b) Absorbance signals of histidine and broadband sensing enhancement factors for $\eta = 0.6$. The device parameters are $p = 105$ μm, $w_1 = w_3 = 26.25$ μm, $h_1 = 35$ μm, and h_2 changes from 0 to 200 μm at intervals of 5 μm. (c) Real part of conductivity σ for a 20 nm thick Mo-based MXene film. (d) Absorbance envelopes of MXene and broadband sensing enhancement factors for $\eta = 0.6$. The device parameters are $p = 200$ μm, $w_1 = w_3 = 50$ μm, $h_1 = 60$ μm, and h_2 changes from 0 μm to 350 μm at intervals of 5 μm.

η decreasing. The results imply that the large electric field along the surface of the metagrating leads to higher absorbance. For $\eta = 1$, the feature at the frequency of 2.37 THz is not sufficient to distinguish. When the asymmetry parameter is reduced to 0.4, the fingerprint feature peak at the frequency of 2.24 THz is truncated. This is because a too small η leads to excessive absorption enhancement in the frequency range from 2.233 to 2.266 THz, and one fails to identify the resonance peaks and cannot retrieve the fingerprint envelope effectively. In contrast, the fingerprint of histidine is effectively retrieved for the asymmetry parameters of 0.8 and 0.6, respectively. They demonstrate the relatively comprehensive wideband fingerprint information of trace histidine. Particularly, compared with $\eta = 0.8$, the tiny fingerprint peaks at frequencies of 2.58 and 2.66 THz are more explicit for $\eta = 0.6$. In the entire frequency range from 2.05 to 2.75 THz, the minimum enhancement factor for $\eta = 0.6$ is 22.84 dB. To evaluate the universality of the metasensor, we further investigate the fingerprint detection for an ultra-thin Mo-based MXene ($Mo_2Ti_2C_3T_z$) material 20 nm thick. Currently, this material is attractive for a variety of sensing and optoelectronic applications [39]. Its optical conductivity indicates a feature peak at the frequency of 1.135 THz, as shown in Fig. 7(c). We also retrieve the absorbance envelopes for

different η values in Fig. 7(d). The absorbance signal becomes larger with η decreasing from 1 to 0.4. The absorbance peaks at the frequency of 1.135 THz for η values of 1, 0.8, and 0.6 indicate that the metasensor can effectively detect the Mo-based MXene. Similar to Fig. 7(b), the fingerprint feature of Mo-based MXene for $\eta = 0.4$ cannot be retrieved clearly in the frequency range from 1.13 to 1.14 THz due to the over absorption enhancement. $\eta = 0.6$ denotes the optimal asymmetry parameter, which exhibits broadband fingerprint signal enhancement factors of over 22.47 dB in Fig. 7(d). Therefore, the above results indicate that there can be an optimal asymmetry parameter for enhanced THz fingerprint metasensing. By a systematic design of the metastructure, one can not only retrieve the broadband THz molecular fingerprint, but also capture the detailed tiny fingerprint features. The thickness-multiplexed metasensing under normal incidence illuminates a simple way without angular manipulation for high-performance THz fingerprint detection of trace samples.

Finally, to indicate the novelty and importance of the proposed devices, we compare their performance with previous studies in Table 1. For a more comprehensive comparison, we also detect 1 μm thick α-lactose based on the thickness-multiplexed sensing method (see details in Appendix C). As observed in Table 1, our thickness-multiplexed and angle-multiplexed metasensors provide the largest peak enhancement times of 308 and 330, respectively, which are much higher than previous work. In view of practical applications, we also consider optical loss in the proposed metagratings, and investigate its influences on THz fingerprint sensing (see details in Appendix D). The simulated results clearly imply the feasibility and reliability of our metasensing scheme in practice.

4. CONCLUSION

In summary, we propose THz trace molecular fingerprint metasensing on a planar surface based on the use of multiplexed quasi-BIC modes, which are manipulated by changing the incident angle or the structural geometry parameter. The sensing enhancement is attributed to the use of evanescent waves at the planar air–metastructure interface for a series of quasi-BIC resonance modes. The broadband fingerprint signals of trace analytes can be retrieved by tuning the reflectance peaks. The coating of samples on a planar sensing surface is more flexible than that directly on the patterned metastructure surface, especially for detecting ultra-thin trace analytes of various physical states or morphologies. By tuning the asymmetry parameter for quasi-BIC modes, one can boost sensing performance significantly. Our study provides a universal planar surface sensing scheme with exceptional enhancement of THz fingerprint

Table 1. Fingerprint Detection Performance of Dielectric Metasensors

| Reference	Metastructure	Sensing Surface	Analyte	Multiplexed Scheme	Spectral Range	Peak Enhancement Times
[15]	Pair pillars	Patterned	Protein A/G	Geometry	Mid-IR	~60
[16]	Pair pillars	Patterned	PMMA	Angle	Mid-IR	~50
[40]	Metagrating	Patterned	hBN	Angle	Mid-IR	~34
[5]	Metagrating	Patterned	α-lactose	Angle	THz	~13
Our work	Inverted metagrating	Planar	α-lactose	Geometry/angle	THz	~308/~330

features, which will facilitate the development of ultrasensitive THz sensors for various trace samples.

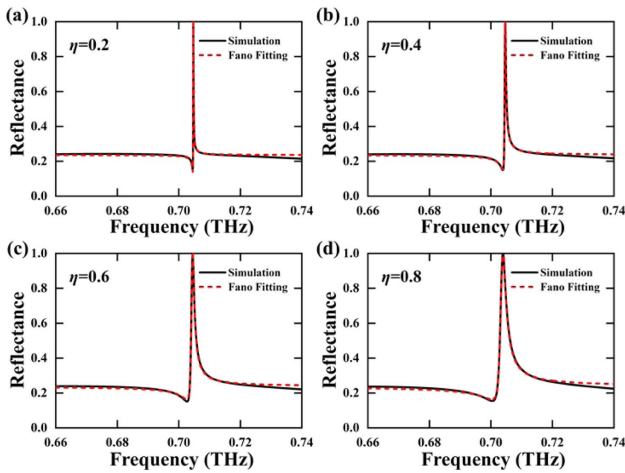## APPENDIX A: FANO FITTING AND QUALITY FACTOR CALCULATION

To extract the Q-factors of quasi-BIC modes, the simulated reflectance spectra are fitted by the Fano theory, as shown in Fig. 8. The fitted curves are consistent with the simulation results for different η values. More details of the fitting parameters are listed in Table 2.

APPENDIX B: EFFECTS OF THICKNESS h_2 ON SENSING PERFORMANCE BASED ON ANGLE-MULTIPLEXED METASENSING

We perform a series of simulations with different values of h_2 based on angle-multiplexed metasensing. Figure 9(a) implies that the peak frequency decreases as h_2 increases from 120 to 250 μm under normal incidence. The normalized electric field distributions of different h_2 illuminate the similar features of evanescent waves. The reflectance spectra and peak envelopes R_s for different values of h_2 with 1 μm thick α-lactose coating are plotted in Fig. 9(b). All envelopes have a dip at
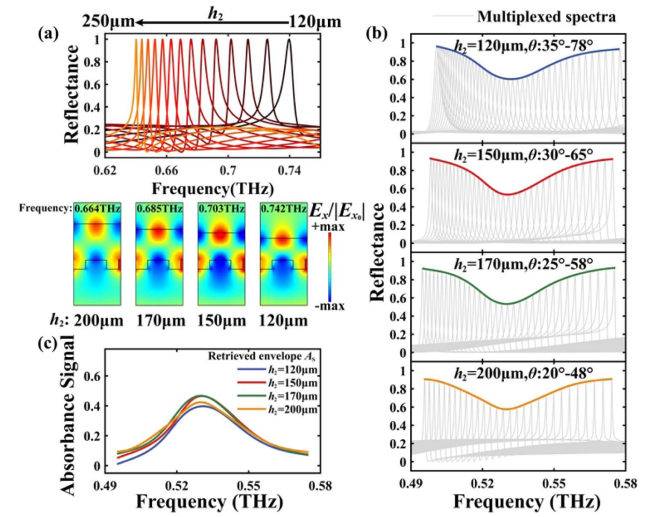
Fig. 9. (a) Reflectance spectra with different thicknesses h_2 and normalized electric field distributions at resonance frequencies under normal incidence. (b) Angle-multiplexed reflectance spectra and envelopes of coating 1 μm thick α-lactose on the metasensor. (c) Absorbance envelopes with different thicknesses h_2. For all simulations, the metastructure parameters are $p = 260$ μm, $\eta = 0.8$, $w_1 = w_3 = 65$ μm, $w_2 = 117$ μm, $w_4 = 13$ μm, and $h_1 = 50$ μm.

around 0.53 THz, corresponding to the maximum absorption frequency of α-lactose. Notably, the angular manipulating range varies with h_2 changing. This demonstrates that the angle-multiplexed metasensing scheme can effectively retrieve the molecular fingerprint for different h_2. The calculated absorbance signals in Fig. 9(c) imply that the absorption intensities for h_2 values of 150 and 170 μm are larger than those of 120 and 200 μm. Hence, we can tune h_2 for specific analytes to optimize the sensing performance for the actual measurement.

APPENDIX C: ABSORPTION ENHANCEMENT OF α-LACTOSE BASED ON THICKNESS-MULTIPLEXED METASENSING

Here, we analyze the absorbance enhancement based on thickness-multiplexed metasensing. Figure 10(a) provides the fingerprint absorbance spectrum for α-lactose of different thicknesses by the conventional sensing method. The metasensing enhances the fingerprint signals of the 1 μm α-lactose

Fig. 8. Simulated reflectance spectra and Fano fitting for (a) $\eta = 0.2$, (b) $\eta = 0.4$, (c) $\eta = 0.6$, and (d) $\eta = 0.8$.

Table 2. Fano Fitting Parameters for the Quasi-BICs of Proposed Metastructures with Different η Values

η	R_0	C_0	q	$\omega_0/(2\pi)$ (THz)	$\tau/(2\pi)$ (THz)	Q
0.05	0.11020	0.12550	2.52	0.70474	8.30×10^{-6}	84,908
0.1	0.11594	0.11797	2.81	0.70475	2.38×10^{-5}	29,574
0.2	0.13522	0.09987	2.84	0.70473	1.21×10^{-4}	5824
0.3	0.12343	0.11237	2.48	0.70464	2.77×10^{-4}	2541
0.4	0.15125	0.08469	3.01	0.70460	4.69×10^{-4}	1502
0.5	0.17046	0.06536	3.45	0.70455	7.44×10^{-4}	946
0.6	0.16218	0.07438	3.23	0.70435	1.09×10^{-3}	646
0.7	0.15535	0.08665	2.93	0.70397	1.52×10^{-3}	463
0.8	0.16081	0.07633	3.19	0.70363	2.04×10^{-3}	344
0.9	0.17013	0.06579	3.43	0.70291	2.04×10^{-3}	251
1	0.17358	0.06129	3.56	0.70141	4.00×10^{-3}	175
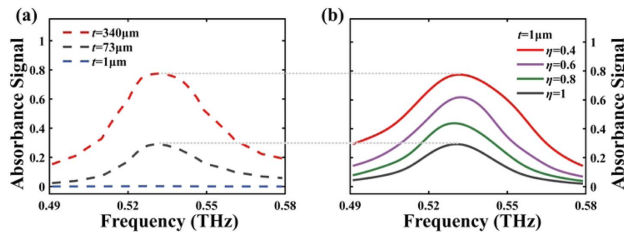
**Fig. 10.** (a) Absorbance spectra of α-lactose with different thicknesses by conventional sensing. (b) Retrieved absorbance signals of 1 μm α-lactose by the thickness-multiplexed metasensing method. The normal incidence of THz waves is applied on the metastructure, whose parameters are $p = 500$ μm, $w_1 = w_3 = 125$ μm, $w_2 = 225$ μm, $w_4 = 25$ μm, $h_1 = 128$ μm, and h_2 changes from 65 to 600 μm at intervals of 5 μm.

layer, as observed in Fig. 10(b). When η decreases from 1 (GMR) to 0.4 (quasi-BIC), the absorbance at 0.53 THz rises from 29.3% to 77.4%. The metasensing for $\eta = 0.4$ demonstrates 308 times enhancement at the fingerprint feature point.

APPENDIX D: FINGERPRINT DETECTION BASED ON LOSSY METAGRATINGS

The loss in all-dielectric metagratings should be considered in practical applications. Hence, we perform a series of simulations based on the lossy metastructures. The THz optical parameters of SiO_2, Topas, and trans-decalin are obtained from the literature [24,34,35]. The detection results imply that the optical signal intensities before and after trace sample coating
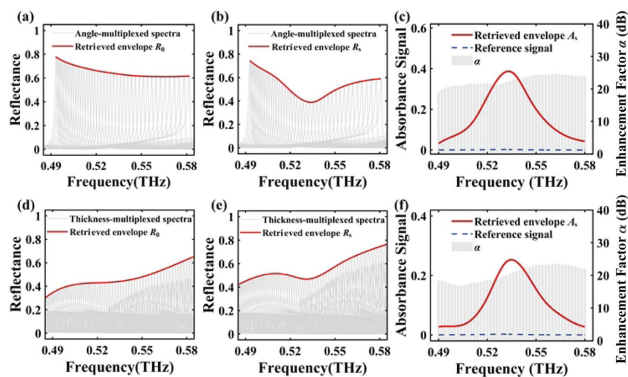
Fig. 11. (a) Angle-multiplexed reflectance spectra and envelope R_0 for an unloaded lossy metasensor. (b) Angle-multiplexed reflectance spectra and envelope of coating 1 μm thick α-lactose on the metasensor. (c) Absorbance signals and broadband sensing enhancement factors. The metastructure parameters are $p = 260$ μm, $\eta = 0.8$, $w_1 = w_3 = 65$ μm, $w_2 = 117$ μm, $w_4 = 13$ μm, $h_1 = 50$ μm, $h_2 = 150$ μm, and θ changes from 28° to 70°. (d) Thickness-multiplexed reflectance spectra and envelope R_0 for an unloaded lossy metasensor. (e) Thickness-multiplexed reflectance spectra and envelope of coating 1 μm thick α-lactose on the metasensor. (f) Absorbance signals and broadband sensing enhancement factors. The normal incidence of THz wave is applied on the metastructure, whose parameters are $p = 500$ μm, $\eta = 0.8$, $w_1 = w_3 = 125$ μm, $w_2 = 225$ μm, $w_4 = 25$ μm, $h_1 = 128$ μm, and h_2 changes from 65 to 600 μm at intervals of 5 μm.

are both decreased, as shown in Figs. 11(a), 11(b), 11(d), and 11(e). This is attributed to the optical loss in dielectric materials. Nevertheless, the fingerprint absorbance signals can be effectively retrieved, as observed in Figs. 11(c) and 11(f). The retrieved fingerprint signals are also enhanced in a broad THz band. The simulation results demonstrate that our method can be applied on lossy metastructures.

Disclosures. The authors declare no conflicts of interest.

Data Availability. Data underlying the results presented in this paper may be obtained from the authors upon reasonable request.

REFERENCES

1. W. J. Choi, K. Yano, M. Cha, F. M. Colombari, J.-Y. Kim, Y. Wang, S. H. Lee, K. Sun, J. M. Kruger, A. F. de Moura, and N. A. Kotov, "Chiral phonons in microcrystals and nanofibrils of biomolecules," Nat. Photonics **16**, 366–373 (2022).
2. R. Damari, O. Weinberg, D. Krotkov, N. Demina, K. Akulov, A. Golombek, T. Schwartz, and S. Fleischer, "Strong coupling of collective intermolecular vibrations in organic materials at terahertz frequencies," Nat. Commun. **10**, 3248 (2019).
3. X. Yang, X. Zhao, K. Yang, Y. Liu, Y. Liu, W. Fu, and Y. Luo, "Biomedical applications of terahertz spectroscopy and imaging," Trends Biotechnol. **34**, 810–824 (2016).
4. S. Ding, J.-Y. Ou, L. Du, L. Zhu, S. A. Khan, H. Chen, and J. Zhu, "Enhancing ultra-wideband THz fingerprint sensing of unpatterned 2D carbon-based nanomaterials," Carbon **179**, 666–676 (2021).
5. J. Zhu, S. Jiang, Y. Xie, F. Li, L. Du, K. Meng, L. Zhu, and J. Zhou, "Enhancing terahertz molecular fingerprint detection by a dielectric metagrating," Opt. Lett. **45**, 2335–2338 (2020).
6. S. Shen, X. Liu, Y. Shen, J. Qu, E. Pickwell-MacPherson, X. Wei, and Y. Sun, "Recent advances in the development of materials for terahertz metamaterial sensing," Adv. Opt. Mater. **10**, 2101008 (2022).
7. M. Seo and H.-R. Park, "Terahertz biochemical molecule-specific sensors," Adv. Opt. Mater. **8**, 1900662 (2020).
8. W. Xu, L. Xie, and Y. Ying, "Mechanisms and applications of terahertz metamaterial sensing: a review," Nanoscale **9**, 13864–13878 (2017).
9. S.-H. Lee, D. Lee, M. H. Choi, J.-H. Son, and M. Seo, "Highly sensitive and selective detection of steroid hormones using terahertz molecule-specific sensors," Anal. Chem. **91**, 6844–6849 (2019).
10. H. M. Silalahi, Y.-P. Chen, Y.-H. Shih, Y.-S. Chen, X.-Y. Lin, J.-H. Liu, and C.-Y. Huang, "Floating terahertz metamaterials with extremely large refractive index sensitivities," Photon. Res. **9**, 1970–1978 (2021).
11. S. A. Khan, N. Z. Khan, Y. Xie, M. T. Abbas, M. Rauf, I. Mehmood, M. Runowski, S. Agathopoulos, and J. Zhu, "Optical sensing by metamaterials and metasurfaces: from physics to biomolecule detection," Adv. Opt. Mater. **10**, 2200500 (2022).
12. A. John-Herpin, A. Tittl, L. Kuhner, F. Richter, S. H. Huang, G. Shvets, S.-H. Oh, and H. Altug, "Metasurface-enhanced infrared spectroscopy: an abundance of materials and functionalities," Adv. Mater. **10**, 2110163 (2022).

13. K. Koshelev and Y. Kivshar, "Dielectric resonant metaphotonics," ACS Photon. **8**, 102–112 (2021).

14. S. Romano, G. Zito, S. Torino, G. Calafiore, E. Penzo, G. Coppola, S. Cabrini, I. Rendina, and V. Mocella, "Label-free sensing of ultralow-weight molecules with all-dielectric metasurfaces supporting bound states in the continuum," Photon. Res. **6**, 726–733 (2018).

15. A. Tittl, A. Leitis, M. Liu, F. Yesilkoy, D.-Y. Choi, D. N. Neshev, Y. S. Kivshar, and H. Altug, "Imaging-based molecular barcoding with pixelated dielectric metasurfaces," Science **360**, 1105–1109 (2018).

16. A. Leitis, A. Tittl, M. Liu, B. H. Lee, M. B. Gu, Y. S. Kivshar, and H. Altug, "Angle-multiplexed all-dielectric metasurfaces for broadband molecular fingerprint retrieval," Sci. Adv. **5**, eaaw2871 (2019).

17. C. W. Hsu, B. Zhen, J. Lee, S.-L. Chua, S. G. Johnson, J. D. Joannopoulos, and M. Soljacic, "Observation of trapped light within the radiation continuum," Nature **499**, 188–191 (2013).

18. K. Koshelev, A. Bogdanov, and Y. Kivshar, "Meta-optics and bound states in the continuum," Sci. Bull. **64**, 836–842 (2019).

19. W. Shi, J. Gu, X. Zhang, Q. Xu, J. Han, Q. Yang, L. Cong, and W. Zhang, "Terahertz bound states in the continuum with incident angle robustness induced by a dual period metagrating," Photon. Res. **10**, 810–819 (2022).

20. S. I. Azzam and A. V. Kildishev, "Photonic bound states in the continuum: from basics to applications," Adv. Opt. Mater. **9**, 2001469 (2021).

21. K. Koshelev, S. Lepeshov, M. Liu, A. Bogdanov, and Y. Kivshar, "Asymmetric metasurfaces with high-*Q* resonances governed by bound states in the continuum," Phys. Rev. Lett. **121**, 193903 (2018).

22. Z. Liu, Y. Xu, Y. Lin, J. Xiang, T. Feng, Q. Cao, J. Li, S. Lan, and J. Liu, "High-*Q* quasibound states in the continuum for nonlinear metasurfaces," Phys. Rev. Lett. **123**, 253901 (2019).

23. F. Wu, J. Wu, Z. Guo, H. Jiang, Y. Sun, Y. Li, J. Ren, and H. Chen, "Giant enhancement of the Goos-Hanchen shift assisted by quasi-bound states in the continuum," Phys. Rev. Appl. **12**, 014028 (2019).

24. M. Naftaly and R. E. Miles, "Terahertz time-domain spectroscopy of silicate glasses and the relationship to material properties," J. Appl. Phys. **102**, 043517 (2007).

25. J. Qiu, X. Liu, Z. Liang, and J. Zhu, "Ultra-wideband perfect reflection and tunneling by all-dielectric metamaterials," Opt. Lett. **46**, 849–852 (2021).

26. S. S. Wang and R. Magnusson, "Theory and applications of guided-mode resonance filters," Appl. Opt. **32**, 2606–2613 (1993).

27. A. Yariv and P. Yeh, *Optical Waves in Crystals* (Wiley, 1984), Vol. **5**.

28. M. F. Limonov, M. V. Rybin, A. N. Poddubny, and Y. S. Kivshar, "Fano resonances in photonics," Nat. Photonics **11**, 543–554 (2017).

29. E. Melik-Gaykazyan, K. Koshelev, J.-H. Choi, S. S. Kruk, A. Bogdanov, H.-G. Park, and Y. Kivshar, "From Fano to quasi-BIC resonances in individual dielectric nanoantennas," Nano Lett. **21**, 1765–1771 (2021).

30. C. Zhou, S. Li, Y. Wang, and M. Zhan, "Multiple toroidal dipole Fano resonances of asymmetric dielectric nanohole arrays," Phys. Rev. B **100**, 195306 (2019).

31. Y. Cai, J. Zhu, and Q. H. Liu, "Tunable enhanced optical absorption of graphene using plasmonic perfect absorbers," Appl. Phys. Lett. **106**, 043105 (2015).

32. A. Roggenbuck, H. Schmitz, A. Deninger, I. C. Mayorga, J. Hemberger, R. Guesten, and M. Grueninger, "Coherent broadband continuous-wave terahertz spectroscopy on solid-state samples," New J. Phys. **12**, 043017 (2010).

33. X. Xing, L. Zhao, Z. Zhang, L. Fang, Z. Fan, X. Liu, X. Lin, J. Xu, J. Chen, X. Zhao, Z. Jin, and G. Ma, "Photoinduced terahertz conductivity and carrier relaxation in thermal-reduced multilayer graphene oxide films," J. Phys. Chem. C **121**, 2451–2458 (2017).

34. P. D. Cunningham, N. N. Valdes, F. A. Vallejo, L. M. Hayden, B. Polishak, X.-H. Zhou, J. Luo, A. K.-Y. Jen, J. C. Williams, and R. J. Twieg, "Broadband terahertz characterization of the refractive index and absorption of some important polymeric and organic electro-optic materials," J. Appl. Phys. **109**, 043505 (2011).

35. M. Afsar and G. Chantry, "Precise dielectric measurements of low-loss materials at millimeter and submillimeter wavelengths," IEEE Trans. Microw. Theory Tech. **25**, 509–512 (1977).

36. https://www.2spi.com/item/4108psn-ba/.

37. W. H. Fissell, A. Dubnisheva, A. N. Eldridge, A. J. Fleischman, A. L. Zydney, and S. Roy, "High-performance silicon nanopore hemofiltration membranes," J. Membr. Sci. **326**, 58–63 (2009).

38. W. N. Wang, W. M. Yue, H. T. Yan, C. L. Zhang, and G. Z. Zhao, "THz time-domain spectroscopy of amino acids," Chin. Sci. Bull. **50**, 1561–1565 (2005).

39. G. Lui, V. Natu, T. Shi, M. W. Barsoum, and L. V. Titova, "Two-dimensional MXenes $Mo_2Ti_2C_3T_z$ and $Mo_2TiC_2T_z$: microscopic conductivity and dynamics of photoexcited carriers," ACS Appl. Energy Mater. **3**, 1530–1539 (2020).

40. Y. Xie, X. Liu, F. Li, J. Zhu, and N. Feng, "Ultra-wideband enhancement on mid-infrared fingerprint sensing for 2D materials and analytes of monolayers by a metagrating," Nanophotonics **9**, 2927–2935 (2020).